Geophysical Research Letters

Nonthermal Limit of Monoenergetic Precipitation in the Auroral Acceleration Region

Spencer M. Hatch[1] [ID]**, Christopher C. Chaston[2]** [ID]**, and James LaBelle[1]** [ID]

[1]Department of Physics and Astronomy, Dartmouth College, Hanover, NH, USA, [2]Space Sciences Laboratory, University of California, Berkeley, CA, USA

Abstract We report statistics from FAST satellite observations revealing the prevalence of nonthermal monoenergetic electron distributions within and below the auroral acceleration region (AAR), and over 21–24 magnetic local time. The energy spectra of intra-AAR auroral primaries reveal a probability distribution of κ ("kappa") values that is "piled up" against a lower bound, $\kappa \gtrsim \kappa_t \simeq 2.45$. The measurements are recorded in the lower reaches of the AAR, as determined from simultaneous upward ion beams, and are therefore unaffected by processes at lower altitudes that may alter auroral primary distributions. We show evidence that the κ values below the AAR tend to be greater than those within the AAR, which suggests that auroral primaries evolve toward thermal equilibrium as they move toward the ionosphere. Only for ~4% of the reported events corresponding to $\kappa \leq \kappa_t$ does a kappa current density-voltage relationship differ appreciably from the classical Maxwellian current density-voltage relationship.

Plain Language Summary Many natural plasmas are extremely rarefied (i.e., collisions between individual charged particles are infrequent) and the motion of the charged particles that comprise them may be highly ordered or correlated. Since one definition of thermal equilibrium is perfectly uncorrelated motion, such ordered motion demonstrates that these plasmas are not strictly in thermal equilibrium. The degree of nonthermality is indicated by the κ ("kappa") index in space physics and is important because it modifies, for example, plasma resonant frequencies and how/where the energy of a precipitating plasma is deposited in the ionosphere. Satellites and ionospheric sounding rockets that measure properties of magnetospheric plasmas have observed κ indices indicating that magnetospheric plasmas are out of thermal equilibrium. However, measurements of κ in the ionosphere are uncertain because magnetospheric precipitation collides with dense ionospheric plasmas. From observations made by the Fast Auroral SnapshoT Explorer (FAST) satellite above the ionosphere, which are free from the effects of low-altitude collisions, we report statistics of the κ index evincing a "pile-up" near $\kappa = 2.45$, which is strong evidence of a presently unknown mechanism for driving magnetospheric precipitation out of thermal equilibrium. These results therefore expose an important deficiency in current understanding of the auroral acceleration process.

1. Introduction

Among the most widely known and frequently employed predictions of classical statistical physics is the distribution of velocities of a thermally equilibrated three-dimensional gas,

$$f_M(E; T, n) = n \left(\frac{m}{2\pi T} \right)^{\frac{3}{2}} e^{-E/T}, \tag{1}$$

otherwise known as the Maxwellian distribution in plasma physics. The plasma density n and temperature T (in energy units) are the only two parameters of this distribution. In plasmas that are well described by a Maxwellian distribution, an overall tendency toward thermal equilibrium is ensured by particle-particle collision rates that are high relative to typical ranges of frequencies over which such plasmas vary and/or are driven (St-Maurice & Schunk, 1979).

In contrast, planetary and astrophysical plasmas that are subject to low collision frequencies, nonlinear or high-frequency forcing, admixture with other populations, or any combination of these conditions, are routinely in stationary (i.e., approximately invariant over relevant time scales) states out of thermal equilibrium (e.g., Livadiotis & McComas, 2010; St-Maurice & Schunk, 1979; Treumann, 1999a; Tsurutani & Lakhina, 1997).

The correlated motion of constituents that accompanies these stationary states appears in processes exhibiting self-similar, or fractal, scales (West & Shlesinger, 1990); hence, their connection with turbulence and scale invariance (Leubner, 2004; Treumann, 1999a).

The degree to which a plasma is out of thermal equilibrium may be modeled with a kappa distribution,

$$f_\kappa(E; T, n, \kappa) = n \left(\frac{m}{2\pi(\kappa - \frac{3}{2})T} \right)^{\frac{3}{2}} \frac{\Gamma(\kappa + 1)}{\Gamma\left(\kappa - \frac{1}{2}\right)} \left(1 + \frac{E}{\left(\kappa - \frac{3}{2}\right)T} \right)^{-1-\kappa}, \tag{2}$$

where the parameter $\kappa \in [\kappa_{\min}, \infty)$ is related to the degree $\rho = \frac{3}{2\kappa} \in [0, 1]$ to which particle motions are correlated (Livadiotis & McComas, 2011). The limit $\kappa \to \infty$ ($\rho = 0$) corresponds to the Maxwellian distribution (1), while the theoretical minimum for a three-dimensional distribution $\kappa_{\min} = 1.5$ ($\rho = 1$) corresponds to perfectly correlated particle motion. From this standpoint Livadiotis and McComas (2010) describe the κ parameter as the "thermodynamic distance" between a given stationary, nonequilibrium state, and thermodynamic equilibrium. Via review of observational literature as well as analysis of the entropy of the kappa distribution, these authors demonstrate that $\kappa_t \simeq 2.45$ ($\rho \simeq 0.61$) marks an apparent transition between stationary states that are far from thermal equilibrium, $\kappa \in [\kappa_{\min}, \kappa_t)$, and "near-equilibrium" states for which $\kappa \in [\kappa_t, \infty)$.

From the standpoint of nonextensive statisical mechanics, the kappa distribution (2) and alternate forms (Bian et al., 2014; Leubner, 2002; Livadiotis & McComas, 2009) are derivable from Tsallis entropy, itself mathematically identical to the largely neglected (Rathie & Silva, 2008) information-theoretical α-entropy introduced by Havrda and Charvát (1967). The kinetic and thermodynamic definitions of temperature T are consistent for the form (2) but may be inconsistent for other forms (Livadiotis & McComas, 2009, 2010).

The earliest instance of a mechanism for driving stationary, nonequilibrium plasma states was given by Scudder and Olbert (1979), who showed that Coulomb collisions between solar wind electrons that undergo diffusion in velocity space exhibit power law-like features in the high-energy tail of the velocity distribution. Hasegawa et al. (1985) showed that similar effects appear in velocity distributions of plasmas subject to superthermal radiation. A host of other mechanisms for driving such nonstationary states exist (e.g., Treumann, 1999a, as well as reviews by St-Maurice & Schunk, 1979, and Pierrard & Lazar, 2010, and references therein), including the interaction of electrons with turbulent Alfvén or broadband lower hybrid waves (Leubner, 2000). Many of these mechanisms are instances of a more general process by which superdiffusivity arises in a geometrically constrained, crowded driven physical system (Bénichou et al., 2013).

Plasma sheet observations of electron and ion distributions better described by a non-Maxwellian distribution were first reported over two decades ago by Christon et al. (1989, 1991), followed shortly thereafter by reports at low (<1,000 km) altitudes (Wing & Newell, 1998) and in the high-latitude plasma sheet (Kletzing et al., 2003). At lower altitudes previous studies of precipitating electrons in or below the magnetosphere-ionosphere transition region that involve kappa distributions (Kaeppler et al., 2014; McIntosh & Anderson, 2014; Ogasawara et al., 2006, 2017; Olsson & Janhunen, 1998) have reported $\kappa \geq \kappa_t$, values that are within the "near-equilibrium" regime (Livadiotis & McComas, 2010), meaning the distributions do not strongly deviate from a Maxwellian distribution. In each of these studies based on low-altitude observations the effects of processes within or near the ionosphere are complicating factors in the determination of source parameters.

In this Letter we report statistics of the degree of nonthermality (i.e., κ) of monoenergetic electron precipitation, which are derived from in situ premidnight AAR observations that are free from the effects complicating studies at lower altitudes. These statistics demonstrate (i) that the majority (~96%) of intra-AAR electron distributions that are best described by a kappa distribution correspond to $\kappa \gtrsim \kappa_t$; (ii) that relative to the distribution of intra-AAR κ values, the distribution of κ values inferred from observations beneath the AAR is shifted to higher values, which indicates evolution of auroral primaries toward thermal equilibrium; (iii) a form of the distribution of κ values that suggests that intra-AAR electron distributions are driven toward non-Maxwellian forms.

2. Case Study Presentation

During an approximately 80-s interval on 17 January 1997, the FAST satellite observed inverted V electron precipitation (Figures 1a and 1b) and intermittent upgoing ion beams between 10 eV and ~1 keV near mid-
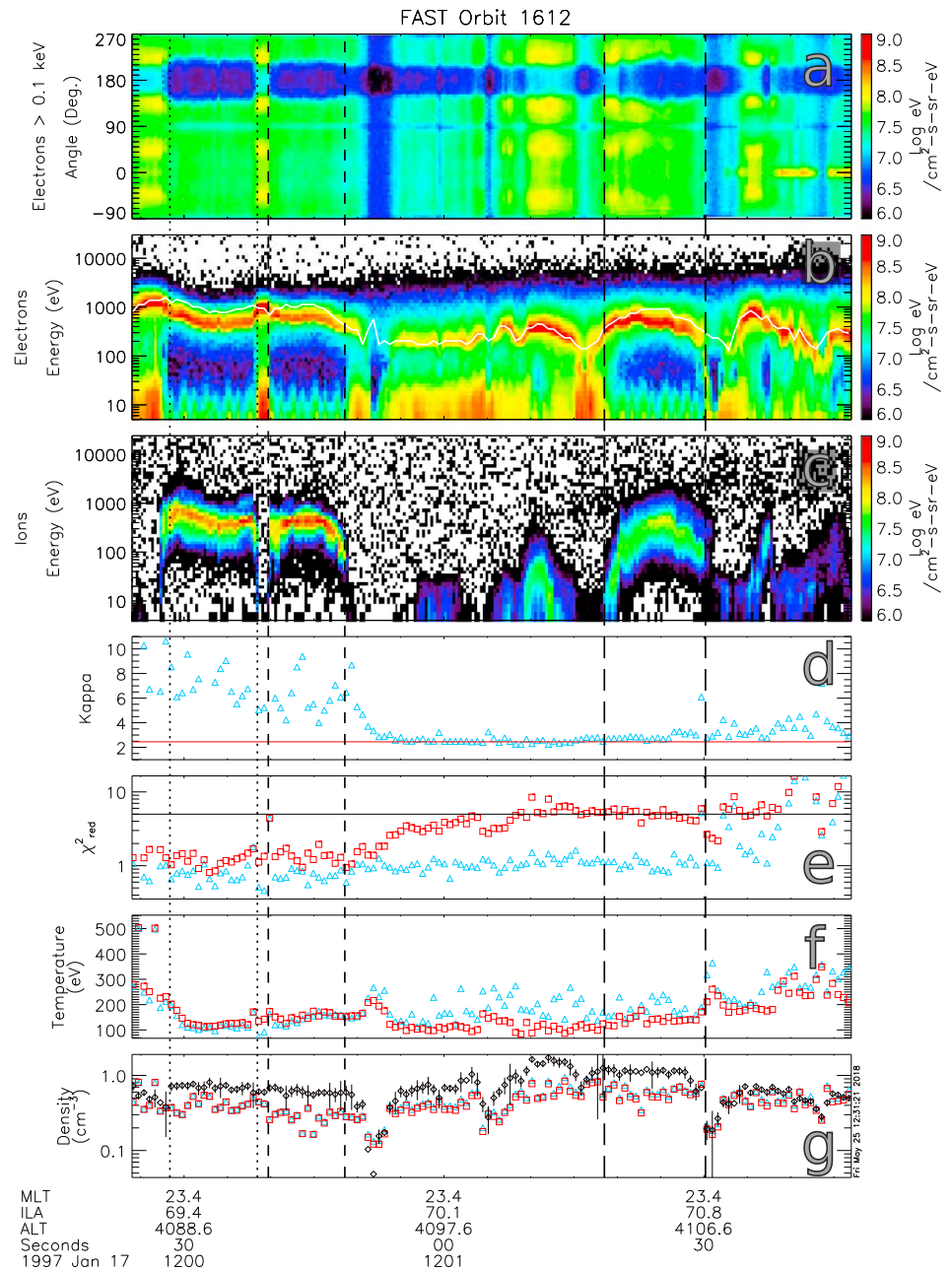
Figure 1. Electron electrostatic analyzer (EESA) observations of inverted V precipitation on 17 January 1997 and corresponding 2-D fit parameters. Parameters related to best-fit Maxwellian and kappa distributions are respectively indicated by red squares and blue triangles in panels (c)–(f). Pairs of dotted and dashed lines indicate periods of upward ion beams, which are automatically identified via the criteria described in Appendix A. (a) >115 eV electron pitch-angle distribution. (b) Average electron energy spectrogram within the earthward loss cone (see text for definition). (c) Ion energy spectrogram within the anti-earthward loss cone. (d) κ fit parameter for the best-fit kappa distribution. (e) Reduced chi-squared statistic χ^2_{red} for each fit type. (f) Best-fit temperatures. (g) Calculated densities (black diamonds) and best-fit densities. Calculated densities are 2-D model-independent moments of the differential flux from 115 eV to 30 keV (the upper bound of the EESA energy range), and over all pitch angles between −90° and 90°. Uncertainties of calculated densities are obtained using analytic expressions for moment uncertainties related to counting statistics for an arbitrary distribution function (Gershman et al., 2015); see Text S1 in the supporting information. EESA observations have been integrated over twice the survey-mode EESA sampling period to improve the related counting statistics.

night magnetic local time (MLT) during a period of low geomagnetic activity ($K_p = 0^-$). Auroral density cavities, which are indicated by low ($< 10^7$ eV/cm^2-s-sr-eV) differential energy flux between ~20 and 200 eV in Figure 1b, are colocated with the upward ion beams visible in Figure 1c. Figure 1b also shows that after ~12:00:54 UT suprathermal tails appear at energies above the monoenergetic peak.

Figure 1a shows that electron distributions observed within these density cavities tend to be isotropic, except over pitch angles within the anti-earthward loss cone. The loss cone is calculated from model geomagnetic field magnitudes at FAST and at the 100-km ionospheric foot point, which are both obtained from International Geomagnetic Reference Field 11.

We perform full 2-D fits to the portion of electron distributions that are observed within the earthward loss cone and between the energy at which the differential energy flux peaks above 115 eV to 30 keV, as measured by FAST electron electrostatic analyzers (EESAs; Carlson et al., 2001). These fits are accomplished using model differential energy flux

$$J_E = \frac{2E^2}{m^2} f\left(E - E_m\right) \tag{3}$$

with the Levenberg-Marquardt weighted least-squares minimization technique. The linearly shifted distribution function $f(E - E_m)$ is either a Maxwellian or kappa distribution, and E_m the energy at which the differential energy flux peaks above 115 eV.

Figure 1d shows the κ parameters that result from this procedure. The red line indicates $\kappa = \kappa_t \simeq 2.45$. Monoenergetic electrons observed prior to 12:00:55 UT are near thermal equilibrium $\kappa \gtrsim 5$, until approximately 12:00:55 UT when κ approaches κ_t. Afterward $\kappa \approx \kappa_t$ until ~12:01:30 UT. Figure 1e shows values of the reduced chi-squared statistic

$$\chi^2_{\text{red}} = \sum_i^N \frac{1}{F} \frac{\left(Y_i(x) - y_i(x)\right)^2}{w_i^2} \tag{4}$$

for 2-D fits using either a kappa distribution (blue triangles) or a Maxwellian distribution (red squares). In this expression i indexes each pitch angle and energy bin, Y_i is the observed differential energy flux, y_i is the differential energy flux of the best-fit model distribution, w_i is the uncertainty due to counting statistics, and F is the total number of pitch angle-energy bins minus the number of free model parameters. Throughout the entire interval shown in Figure 1 χ^2_{red} for the best-fit kappa distribution tends to be less than that for the best-fit Maxwellian distribution. The difference is most pronounced between 12:00:55 UT and 12:01:30 UT, corresponding to the interval during which $\kappa \approx \kappa_t$ in Figure 1d.

Typical ranges of electron densities and temperatures in the plasma sheet are $0.01 - 0.5$ cm^{-3} and $400 - 900$ eV (Kletzing et al., 2003; Paschmann et al., 2003). Figures 1f–1g show that the calculated (black diamonds) densities, as well as best-fit kappa (blue triangles) and Maxwellian (red squares) densities, are within the typical range of densities. Best-fit kappa and Maxwellian temperatures ($90 - 350$ eV) are somewhat below but generally within the typical range.

Figure 2 shows an example of electron observations during $12:00:55 - 12:01:30$ UT. In Figure 2a the 1-D best-fit kappa and Maxwellian distributions (blue dashed line and red dash-dotted line, respectively) overlay the observed distribution (black crosses). The best-fit Maxwellian distribution fails to describe the suprathermal tail ($\chi^2_{\text{red}} = 7.89$), whereas the best-fit kappa distribution describes the suprathermal tail of the observed distribution ($\chi^2_{\text{red}} = 1.43$). Both Maxwellian and kappa best-fit temperatures (96 and 153 eV, respectively) are somewhat low compared to the typical range for the plasma sheet.

The auroral zone crossing presented in Figure 1 shows that the transition from approximately Maxwellian to non-Maxwellian precipitation may take place over time scales of order 10 s and/or distances of order 100 km within the lower reaches of the AAR. This transition is indicated by κ in Figure 1d.

3. Statistical Database

The observations presented in Figure 1d suggest a possible natural boundary near $\kappa \approx \kappa_t$. As we show in what follows, statistical evidence from intra-AAR observations supports the existence of this boundary. The
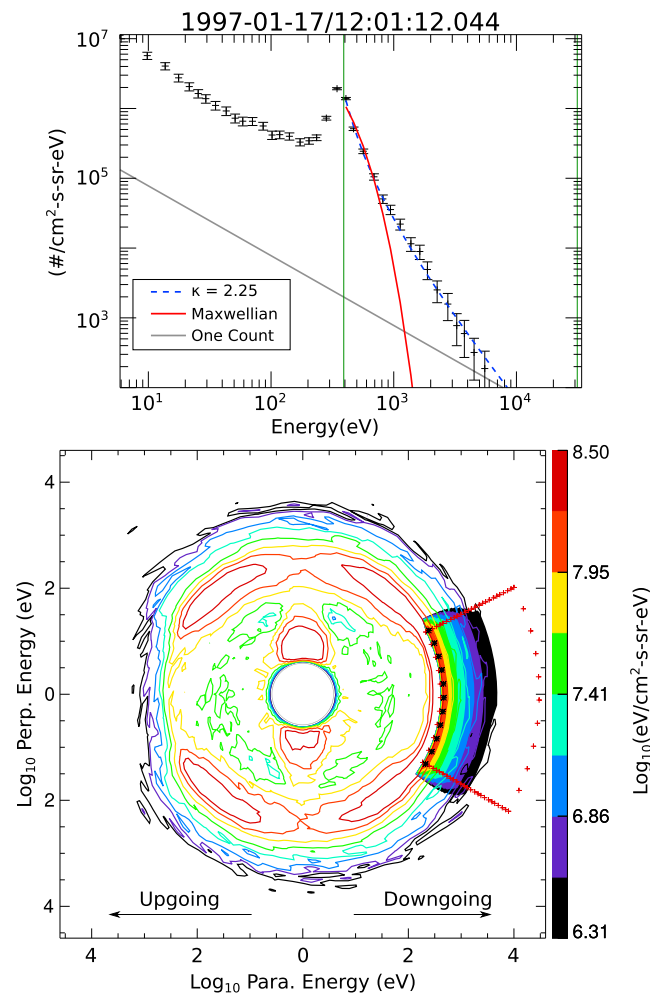
Figure 2. Electron spectra observed at 12:01:12.044 – 12:01:12.674 UT. (a) 1-D average differential number flux spectrum (black crosses) within the earthward loss cone, with best-fit Maxwellian and kappa distributions overlaid (red dash-dotted line and blue dashed line, respectively). The uncertainty of each observed differential number flux is calculated by conversion of the particle count uncertainty $\sqrt{N}$ to units of differential number flux. (b) Best-fit 2-D kappa distribution (solid contours) with the observed 2-D differential energy flux spectrum overlaid (contour lines). For each pitch angle black asterisks indicate the peak energy $E_m = 350$ eV, and red plus signs outline the range of energies and pitch angles used to perform the 2-D fit.

database from which this statistical evidence arises is composed of ∼2.5 years of FAST observations during positively identified traversals of the premidnight AAR.

The starting point in developing the statistical database is the identification of FAST observations of monoenergetic precipitation, which is accomplished using the FAST adaptation of the Newell et al. (2009) criteria for monoenergetic precitation presented by Hatch et al. (2016). With these criteria we identify streaks of monoenergetic precipitation lasting at least 30 s for all FAST observations within 21 – 24 MLT between November 1996 and March 1999. To improve counting statistics we integrate EESA and IESA observations to obtain an effective sample period of 1.25 s. We then perform fits to identified monoenergetic differential energy flux spectra using both Maxwellian and kappa model differential energy flux (3), generating summary figures and plots of individual fits such as those shown in Figures 1 and 2 and additional diagnostic figures (Figure S2). Summary figures are manually examined to ensure quality of the observations and fits. Because the range of inferred potentials varies logarithmically (e.g., Dombeck et al., 2013), adjustments are made to the energy boundaries over which peak detection occurs and distributions are fitted and the fits are rerun as necessary.

Figure 3a plots the quantity $R \equiv \chi^2_{\mathrm{red},M} / \chi^2_{\mathrm{red},\kappa}$ for $N = 31,389$ candidate distribution fits, where $\chi^2_{\mathrm{red},M}$ is the reduced chi-squared statistic for a candidate Maxwellian distribution fit ("Maxwellian fit") and $\chi^2_{\mathrm{red},\kappa}$ the
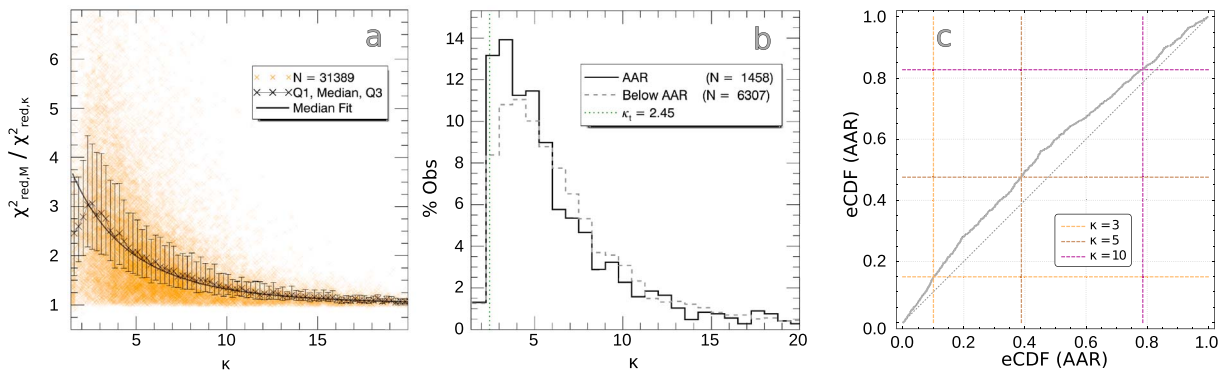
Figure 3. Kappa statistics. (a) Ratio of Maxwellian and kappa reduced chi-squared values for the entire database. Only kappa fits for which $R \equiv \chi^2_{red,M}/\chi^2_{red,\kappa} \geq \hat{R}_{median}$ and $\chi^2_{red,\kappa} \leq 5$ are included in the statistics shown in Figures 3b and 3c. (b) Statistics of κ values within (solid black line) and below (gray dashed line) the AAR. (c) Probability plot (or "p-p plot") of eCDFs formed from the distributions shown in Figure 3b. The gray dashed 45° line indicates the trend followed if the eCDFs were identical. Orange, brown, and purple dashed lines denote the value of each eCDF for $\kappa = 3$, 5, and 10, respectively. AAR = auroral acceleration region.

reduced chi-squared statistic for a candidate kappa distribution fit ("kappa fit"). Within bins of width 0.25, the "x" symbols indicate the median value $R_{median}(\kappa)$, and the lower and upper edges of each error bar indicate the first and third quartile.

For $1.5 < \kappa < 2.5$ the rising trend in R_{median} occurs due to the large number of fits to observations with low counting statistics and therefore high uncertainties. (For instance, the large cluster of points between $\kappa = 1.5$ and $\kappa = 2$ and for $R < 2$ are the outcomes of fitting observed distributions inferred from low EESA count rates.) For $\kappa \geq 2.5$ it is apparent that $R_{median}(\kappa) \rightarrow 1$ and that the spread in R values decreases with increasing κ, as expected since the form of the kappa distribution is approximately Maxwellian for $\kappa \gtrsim 10$. The black line indicates a function of the form $\hat{R}_{median}(\kappa) = (a\kappa + b)^c + 1$ used to fit $R_{median}(\kappa)$ values for $\kappa \geq 2.5$. The best-fit parameters are $a = 0.0569$, $b = 0.718$, and $c = -4.46$.

To ensure the quality of each fit, we use only observations for which (i) $R \geq \hat{R}_{median}(\kappa)$ and (ii) $\chi^2_{red,\kappa} \leq 5$. The latter requirement is imposed based on manual inspection of thousands of individual fits. To remove possible effects related to geomagnetic storms, we also remove all observations corresponding to $Dst < -20$ nT. A total of $N = 7{,}765$ EESA observations with effective sample periods of ≥ 1.25 s meet the foregoing criteria. Last, we separate observations that are positively within the AAR from those that are not. For this study the AAR is operationally defined by the simultaneous presence of a potential structure both above and below FAST. The former is signaled by monoenergetic electron precipitation, as previously described, and the latter by an upward ion beam. To identify upward ion beams in an automated fashion we apply the criteria described in Appendix A, which have been developed based on manual examination of FAST ion beam observations. Applying these criteria to IESA observations during the period described in the previous section results in the pairs of dashed and dotted vertical lines shown in Figure 1, where the period between each pair of lines indicates continuous observations of upward ion beams. (Figure 1c shows that ion beams are present but not indicated during two additional but brief periods, centered near 12:01:11 UT and 12:01:38 UT.)

Figure 3b displays distributions of κ values within (solid black line) and below (dashed gray line) the AAR. For each distribution the percentage of observations very rapidly rises from <2% below $\kappa = 2.25$ to ~10%. The peak of each distribution lies between $\kappa = \kappa_t$ and $\kappa = 5$, while the percentage of observations begins to taper off near $\kappa = 5$. Relative to the distribution of intra-AAR observations, the below-AAR distribution is shifted to higher κ values.

This overall shift is illustrated in Figure 3c, which plots the empirical cumulative distribution function (eCDF) of the intra-AAR distribution as a function of the below-AAR eCDF. The orange lines intersecting at (0.097, 0.152) indicate that ~10% of below-AAR and ~15% of intra-AAR κ values correspond to $\kappa \leq 3$, as is evident in Figure 3b. The purple lines intersecting at (0.387, 0.479) indicate that ~39% of below-AAR and ~48% of intra-AAR κ values correspond to $\kappa \leq 5$.

Regarding the degree of significance of the differences between the intra-AAR and below-AAR distributions, the two-sample Kolmogorov-Smirnov, Anderson-Darling, and Cramér-von Mises tests yield p values less than

2×10^{-12}, and all reject the hypothesis that the intra-AAR and below-AAR distributions are drawn from the same population at the 0.1% level. Forming all possible pairs of κ values from the intra-AAR distribution and κ values from the below-AAR distribution (Kerby, 2014; McGraw & Wong, 1992), we find a 56% probability that κ drawn at random from the intra-AAR distribution is less than κ drawn at random from the below-AAR distribution.

4. Discussion

We find that for 96% of best-fit kappa values inferred from measurements both within and below the AAR the value of the κ parameter is limited to $\kappa \geq \kappa_t$. This range constitutes the "near-equilibrium" regime (Livadiotis & McComas, 2010), or weak to modest deviation from Maxwellian form, and accords with previous in situ observations in the plasma sheet (Christon et al., 1989, 1991; Kletzing et al., 2003) and in or below the magnetosphere-ionosphere transition region (Kaeppler et al., 2014; McIntosh & Anderson, 2014; Ogasawara et al., 2006, 2017; Olsson & Janhunen, 1998). Similar limits have been reported for other astrophysical and planetary plasmas (§4.3 of Livadiotis & McComas, 2010), including Saturnian H^+ distributions measured by Cassini over L shells of $5-20$ R_S (Dialynas et al., 2009) and ^4He distributions measured by the WIND spacecraft (Collier et al., 1996).

Unlike the measurements we report here, none of the previous studies in or below the magnetosphere-ionosphere transition region that involve kappa distributions were performed both within the AAR and unambiguously above auroral arcs. These characteristics tend to eliminate distortion of the primary electron distribution due to collisions and the superposition of multiple electron components prevalent at low altitudes, while unambiguously connecting these electron distributions to the primary electron acceleration process. The importance of these characteristics is illustrated in Figure 3b, which shows that (i) the intra-AAR distribution is "piled up" against $\kappa = \kappa_t$, and (ii) the distribution of κ values below the AAR is shifted toward thermal equilibrium relative to the distribution of intra-AAR κ values.

Regarding uncertainty the kappa statistics in Figure 3b depend on the observed spectral shape of electron precipitation, and therefore on the calibration of FAST EESAs, which rely on microchannel plate (MCP) electron multipliers (Carlson et al., 2001). MCPs suffer a decrease in detection efficiency for electrons at energies near or above 1 keV (Goruganthu & Wilson, 1984; Paschmann et al., 1970). We apply no efficiency calibration to EESA observations. It is therefore possible that the power-law tails are in reality more extreme than observed (J. McFadden, personal communication, July 12, 2018) and the kappa values in Figures 1–3 slightly lower than we have estimated.

The "piling up" of the intra-AAR distribution of κ values near $\kappa = \kappa_t$ indicates a source population in the plasma sheet of the same form and/or the action of processes between the source and the locus of observation that drive particle distributions away from thermal equilibrium (i.e., Maxwellian form). With regard to the latter and with the exception of the work by Leubner (2001), to our knowledge there are no models describing how extended power-law tails on auroral primary distributions/kappa distributions are driven locally within the AAR, nor indeed how such κ values may be attained in the plasma sheet. Stepanova and Antonova (2015) present evidence suggesting turbulence as a cause of low κ values in the plasma sheet, but they do not perform a direct test of this hypothesis.

In a plasma that is described by a kappa distribution the degree to which particle motions are correlated is inversely related to κ. It follows that a process tending to randomize the motion of auroral primaries tends to bring auroral primaries nearer to thermal equilibrium and to increase κ. On the other hand, a process that leads to the availability of free energy in the absence of collisions or in the presence of nonlinear instabilities, or both, instead tends to correlate the motion of auroral primaries (Treumann, 1999b). In this case the distribution of primaries may evolve away from Maxwellian form and κ may decrease. The processes responsible for the observed lower boundary at κ_t in Figure 3b likely represent a balance between these general processes. Nevertheless, the exact physics that leads to nonthermal distributions in the course of auroral acceleration remains unknown, or at best untested. From this standpoint the results in Figure 3b expose an important deficiency in present-day understanding of the auroral acceleration process.

The relative shift between the intra-AAR and below-AAR distributions of κ values indicates that information about the degree of nonthermality of a monoenergetic primary distribution may be lost at lower altitudes,

especially for auroral primaries with κ values near the boundary κ_t. The relative shift to higher kappa values in particular suggests that auroral primaries rapidly evolve toward Maxwellian form after passing through the AAR.

Results in Figures 3b and 3c also have general consequences for posited theoretical relationships between current density and voltage, so-called J-V relations (e.g., Boström, 2003; Dors & Kletzing, 1999; Janhunen & Olsson, 1998; Liemohn & Khazanov, 1998; Pierrard, 1996; Pierrard et al., 2007). These relationships assume a particular form for a magnetospheric source distribution (e.g., Maxwellian, bi-Maxwellian, and kappa), which is mapped via Liouville's theorem along converging field lines and through a potential structure to the ionosphere. Taking the first moment of the mapped distribution yields a prediction for the ionospheric field-aligned current density. The simplest J-V relation (Knight, 1973)

$$j_{\|,M}(\Delta\Phi; T_m, n_m, R_B) = -en_m \left(\frac{T_m}{2\pi m_e} \right)^{\frac{1}{2}} R_B \left[1 - \left(1 - R_B^{-1} \right) \exp\left\{ -\frac{\overline{\phi}}{(R_B - 1)} \right\} \right] \tag{5}$$

assumes a monotonic potential profile and a Maxwellian source distribution. In this expression $\Delta\Phi$ and R_B are respectively the total potential drop and the magnetic mirror ratio between the source region and the ionosphere, T_m and n_m are respectively the source temperature (in units of energy) and density, and m_e is the electron mass. The corresponding J-V relation with a source population described by a kappa distribution, (Dors & Kletzing, 1999)

$$j_{\|,\kappa}(\Delta\Phi; T_m, n_m, \kappa, R_B) = -en_m \left(\frac{(\kappa-\frac{3}{2})T_m}{2\pi m_e} \right)^{\frac{1}{2}} \frac{\Gamma(\kappa+1)}{\Gamma(\kappa-\frac{1}{2})} \frac{R_B}{\kappa(\kappa-1)}$$
$$\times \left[1 - \left(1 - R_B^{-1} \right) \left(1 + \frac{\overline{\phi}}{(\kappa-\frac{3}{2})(R_B-1)} \right)^{-\kappa+1} \right], \tag{6}$$

includes κ as an additional parameter and reduces to the Maxwellian J-V relation (5) for $\kappa \to \infty$.

For equal magnetospheric source density n_m and source temperature T_m the maximum current density predicted by the kappa J-V relation (6) is greater than that predicted by the Maxwellian J-V relation (5). In particular, for equal n_m and T_m the maximum ratio of equations (5) and (6),

$$\text{Max}[R_J] = \text{Max}\left[\frac{j_{\|,\kappa}\left(\Delta\Phi; T_m; n_m; \kappa; R_B \right)}{j_{\|,M}\left(\Delta\Phi; T_m; n_m; R_B \right)} \right], \tag{7}$$

is approximately 1.33 for $\kappa = \kappa_t$ in equation (6). The statistics in Figure 3b indicate that more than 95% of cases correspond to $\kappa \geq \kappa_t$, which suggests that there is an appreciable difference between the Maxwellian J-V relation (5) and the kappa J-V relation (6) in less than 5% of cases. These statistics are however specific to the premidnight region during low geomagnetic activity; possible variations with, for example, local time, latitude, and geomagnetic activity remain to be investigated.

Appendix A: Automated Detection of Ion Beams

For each ion ESA (IESA) observation we calculate the range of pitch angles constituting the anti-earthward portion of the ionospheric loss cone, and reduce this range by a factor of two (e.g., from [150°, 210°] to [165°, 195°] in the Northern Hemisphere). We average IESA observations over this reduced range of pitch angles to obtain the average "upward ion beam" differential energy spectrum ("UIB spectrum"). We also average IESA observations over the 180° range of anti-earthward angles to obtain the average "upward" differential energy spectrum ("UA spectrum"). To avoid spurious ion beam detection due to spacecraft charging, we zero the differential energy flux of any energy channels less than the negative of the spacecraft potential for both the UIB and the UA spectrum.

Let $(\frac{dJ}{dE})_p$ and E_p respectively denote the peak differential energy flux of the UIB spectrum and the energy of the IESA channel in which $(\frac{dJ}{dE})_p$ is detected. The UIB spectrum must meet the following criteria.

- $(\frac{dJ}{dE})_p \geq 10^7$ eV/cm²-s-sr-eV
- For at least one energy channel both above and below E_p, the differential energy flux must be less than $(\frac{dJ}{dE})_p$ by at least 40%. Up to four channels above and up to six channels below E_p are considered, within the bounds of the IESA energy range.
- The differential energy flux within energy channel E_p of the UA spectrum must be at least three times less than $(\frac{dJ}{dE})_p$.
- Both E_p and the average energy of the UIB spectrum must equal or exceed 10 eV. The average energy is the ratio of energy flux and number flux moments; each moment is calculated over the reduced "UIB" range of pitch angles, and over all energies from above the spacecraft potential to the IESA detector limit.

References

Bénichou, O., Bodrova, A., Chakraborty, D., Illien, P., Law, A., Mejía-Monasterio, C., et al. (2013). Geometry-induced superdiffusion in driven crowded systems. *Physical Review Letters*, *111*(260601). https://doi.org/10.1103/PhysRevLett.111.260601

Bian, N. H., Emslie, A. G., Stackhouse, D. J., & Kontar, E. P. (2014). The formation of kappa-distribution accelerated electron populations in solar flares. *The Astrophysical Journal*, *796*(2), 142. https://doi.org/10.1088/0004-637X/796/2/142

Boström, R. (2003). Kinetic and space charge control of current flow and voltage drops along magnetic flux tubes: Kinetic effects. *Journal of Geophysical Research*, *108*(A4), 8004. https://doi.org/10.1029/2002JA009295

Carlson, C. W., Mcfadden, J. P., Turin, P., Curtis, D. W., & Magoncelli, A. (2001). The electron and ion plasma experiment for FAST. *Space Science Reviews*, *98*(1), 33–66. https://doi.org/10.1023/A:1013139910140

Christon, S. P., Williams, D. J., Mitchell, D. G., Frank, L. A., & Huang, C. Y. (1989). Spectral characteristics of plasma sheet ion and electron populations during undisturbed geomagnetic conditions. *Journal of Geophysical Research*, *94*(A10), 13,409–13,424. https://doi.org/10.1029/JA094iA10p13409

Christon, S. P., Williams, D. J., Mitchell, D. G., Huang, C. Y., & Frank, L. A. (1991). Spectral characteristics of plasma sheet ion and electron populations during disturbed geomagnetic conditions. *Journal of Geophysical Research*, *96*(A1), 1–22. https://doi.org/10.1029/90JA01633

Collier, M. R., Hamilton, D. C., Gloeckler, G., Bochsler, P., & Sheldon, R. B. (1996). Neon-20, oxygen-16, and helium-4 densities, temperatures, and suprathermal tails in the solar wind determined with WIND/MASS. *Geophysical Research Letters*, *23*(10), 1191–1194. https://doi.org/10.1029/96GL00621

Dialynas, K., Krimigis, S. M., Mitchell, D. G., Hamilton, D. C., Krupp, N., & Brandt, P. C. (2009). Energetic ion spectral characteristics in the Saturnian magnetosphere using Cassini/MIMI measurements. *Journal of Geophysical Research*, *114*, A01212. https://doi.org/10.1029/2008JA013761

Dombeck, J., Cattell, C., & McFadden, J. (2013). A FAST study of quasi-static structure ("Inverted-V") potential drops and their latitudinal dependence in the premidnight sector and ramifications for the current-voltage relationship. *Journal of Geophysical Research: Space Physics*, *118*, 5731–5741. https://doi.org/10.1002/jgra.50532

Dors, E. E., & Kletzing, C. A. (1999). Effects of suprathermal tails on auroral electrodynamics. *Journal of Geophysical Research*, *104*(A4), 6783–6796. https://doi.org/10.1029/1998JA900135

Gershman, D. J., Dorelli, J. C., Viñas, A. F., & Pollock, C. J. (2015). The calculation of moment uncertainties from velocity distribution functions with random errors. *Journal of Geophysical Research: Space Physics*, *120*, 6633–6645. https://doi.org/10.1002/2014JA020775

Goruganthu, R. R., & Wilson, W. G. (1984). Relative electron detection efficiency of microchannel plates from 0–3 keV. *Review of Scientific Instruments*, *55*(12), 2030–2033. https://doi.org/10.1063/1.1137709

Hasegawa, A., Mima, K., & Duong-van, M. (1985). Plasma distribution function in a superthermal radiation field. *Physical Review Letters*, *54*(24), 2608–2610. https://doi.org/10.1103/PhysRevLett.54.2608

Hatch, S. M., Chaston, C. C., & Labelle, J. (2016). Alfvén wave–driven ionospheric mass outflow and electron precipitation during storms. *Journal of Geophysical Research: Space Physics*, *121*, 7828–7846. https://doi.org/10.1002/2016JA022805

Havrda, J., & Charvát, F. (1967). Quantification method of classification processes: Concept of structural α-entropy. *Kybernetica*, *3*(1), 30–35.

Janhunen, P., & Olsson, A. (1998). The current-voltage relationship revisited: Exact and approximate formulas with almost general validity for hot magnetospheric electrons for bi-Maxwellian and kappa distributions. *Annals of Geophysics*, *16*(3), 292–297. https://doi.org/10.1007/s00585-998-0292-6

Kaeppler, S. R., Nicolls, M. J., Strømme, A., Kletzing, C. A., & Bounds, S. R. (2014). Observations in the E region ionosphere of kappa distribution functions associated with precipitating auroral electrons and discrete aurorae. *Journal of Geophysical Research: Space Physics*, *119*, 10,110–16,4183. https://doi.org/10.1002/2014JA020356

Kerby, D. S. (2014). The simple difference formula: An approach to teaching nonparametric correlation. *Comprehensive Psychology*, *3*, 1. https://doi.org/10.2466/11.IT.3.1

Kletzing, C. A., Scudder, J. D., Dors, E. E., & Curto, C. (2003). Auroral source region: Plasma properties of the high-latitude plasma sheet. *Journal of Geophysical Research*, *108*(A10), 1360. https://doi.org/10.1029/2002JA009678

Knight, S. (1973). Parallel electric fields. *Planetary and Space Science*, *21*, 741–750. https://doi.org/10.1016/0032-0633(73)90093-7

Leubner, M. (2000). Wave induced suprathermal tail generation of electron velocity space distributions. *Planetary and Space Science*, *48*(2-3), 133–141. https://doi.org/10.1016/S0032-0633(99)00091-4

Leubner, M. P. (2001). Energetic tail evolution of auroral electron spectra. *Physics and Chemistry of the Earth, Part C: Solar*, *26*(1-3), 61–64. https://doi.org/10.1016/S1464-1917(00)00091-X

Leubner, M. P. (2002). A nonextensive entropy approach to kappa-distributions. *Astrophysics and Space Science*, *282*(3), 573–579. https://doi.org/10.1023/A:1020990413487

Leubner, M. P. (2004). Fundamental issues on kappa-distributions in space plasmas and interplanetary proton distributions. *Physics of Plasmas*, *11*(4), 1308. https://doi.org/10.1063/1.1667501

Liemohn, M. W., & Khazanov, G. V. (1998). Collisionless plasma modeling in an arbitrary potential energy distribution. *Physics of Plasmas*, *5*(3), 580–589. https://doi.org/10.1063/1.872750

Livadiotis, G., & McComas, D. J. (2009). Beyond kappa distributions: Exploiting Tsallis statistical mechanics in space plasmas. *Journal of Geophysical Research*, *114*, A11105. https://doi.org/10.1029/2009JA014352

Livadiotis, G., & McComas, D. J. (2010). Exploring transitions of space plasmas out of equilibrium. *The Astrophysical Journal*, *714*(1), 971–987. https://doi.org/10.1088/0004-637X/714/1/971

Livadiotis, G., & McComas, D. J. (2011). Invariant kappa distribution in space plasmas out of equilibrium. *The Astrophysical Journal*, *741*(2), 88. https://doi.org/10.1088/0004-637X/741/2/88

McGraw, K. O., & Wong, S. P. (1992). A common language effect size statistic. *Psychological Bulletin*, *111*, 361–365. https://doi.org/10.1037/0033-2909.111.2.361

McIntosh, R. C., & Anderson, P. C. (2014). Maps of precipitating electron spectra characterized by Maxwellian and kappa distributions. *Journal of Geophysical Research: Space Physics*, *119*, 10,116–10,132. https://doi.org/10.1002/2014JA020080

Newell, P. T., Sotirelis, T., & Wing, S. (2009). Diffuse, monoenergetic, and broadband aurora: The global precipitation budget. *Journal of Geophysical Research*, *114*, A09207. https://doi.org/10.1029/2009JA014326

Ogasawara, K., Asamura, K., Takashima, T., Saito, Y., & Mukai, T. (2006). Rocket observation of energetic electrons in the low-altitude auroral ionosphere during the DELTA campaign. *Earth, Planets and Space*, *58*(9), 1155–1163. https://doi.org/10.1186/BF03352005

Ogasawara, K., Livadiotis, G., Grubbs, G. A., Jahn, J.-M., Michell, R., Samara, M., et al. (2017). Properties of suprathermal electrons associated with discrete auroral arcs. *Geophysical Research Letters*, *44*, 3475–3484. https://doi.org/10.1002/2017GL072715

Olsson, A., & Janhunen, P. (1998). Field-aligned conductance values estimated from Maxwellian and kappa distributions in quiet and disturbed events using Freja electron data. *Annals of Geophysics*, *16*(3), 298–302. https://doi.org/10.1007/s00585-998-0298-0

Paschmann, G., Haaland, S., & Treumann, R. (Eds.) (2003). *Theoretical Building Blocks Edited by* Paschmann, G., Haaland, S., & Treumann, R. (pp. \label{}41–92). Netherlands, Dordrecht: Springer. https://doi.org/10.1007/978-94-007-1086-3

Paschmann, G., Shelley, E. G., Chappell, C. R., Sharp, R. D., & Smith, L. F. (1970). Absolute efficiency measurements for channel electron multipliers utilizing a unique electron source. *Review of Scientific Instruments*, *41*(12), 1706–1711. https://doi.org/10.1063/1.1684393

Pierrard, V. (1996). New model of magnetospheric current-voltage relationship. *Journal of Geophysical Research*, *101*(A2), 2669–2675. https://doi.org/10.1029/95JA00476

Pierrard, V., Khazanov, G. V., & Lemaire, J. F. (2007). Current–voltage relationship. *Journal of Atmospheric and Solar-Terrestrial Physics*, *69*(16), 2048–2057. https://doi.org/10.1016/j.jastp.2007.08.005

Pierrard, V., & Lazar, M. (2010). Kappa distributions: Theory and applications in space plasmas. *Solar Physics*, *267*(1), 153–174. https://doi.org/10.1007/s11207-010-9640-2

Rathie, P. N., & Silva, S. D. (2008). Shannon, Lévy, and Tsallis: A note. *Applied Mathematical Sciences*, *2*(28), 1359–1363.

Scudder, J. D., & Olbert, S. (1979). A theory of local and global processes which affect solar wind electrons, 1. The origin of typical 1 AU velocity distribution functions—Steady state theory. *Journal of Geophysical Research*, *84*(A6), 2755–2772. https://doi.org/10.1029/JA084iA06p02755

St-Maurice, J.-P., & Schunk, R. W. (1979). Ion velocity distributions in the high-latitude ionosphere. *Reviews of Geophysics*, *17*(1), 99–134. https://doi.org/10.1029/RG017i001p00099

Stepanova, M., & Antonova, E. E. (2015). Role of turbulent transport in the evolution of the κ distribution functions in the plasma sheet. *Journal of Geophysical Research: Space Physics*, *120*, 3702–3714. https://doi.org/10.1002/2014JA020684

Treumann, R. A. (1999a). Generalized-Lorentzian Thermodynamics. *Physica Scripta*, *59*(3), 204–214. https://doi.org/10.1238/Physica.Regular.059a00204

Treumann, R. A. (1999b). Kinetic theoretical foundation of Lorentzian statistical mechanics. *Physica Scripta*, *59*(1), 19–26. https://doi.org/10.1238/Physica.Regular.059a00019

Tsurutani, B. T., & Lakhina, G. S. (1997). Some basic concepts of wave-particle interactions in collisionless plasmas. *Reviews of Geophysics*, *35*(4), 491–501. https://doi.org/10.1029/97RG02200

West, B. J., & Shlesinger, M. (1990). The Noise in Natural Phenomena. *American Scientist*, *78*(1), 40–45.

Wing, S., & Newell, P. T. (1998). Central plasma sheet ion properties as inferred from ionospheric observations. *Journal of Geophysical Research*, *103*(A4), 6785–6800. https://doi.org/10.1029/97JA02994